Passive Image-Splicing Detection by a 2-D Noncausal Markov Model

Xudong Zhao, *Member, IEEE*, Shilin Wang, *Member, IEEE*, Shenghong Li, *Member, IEEE*, and Jianhua Li

Abstract—In this paper, a 2-D noncausal Markov model is proposed for passive digital image-splicing detection. Different from the traditional Markov model, the proposed approach models an image as a 2-D noncausal signal and captures the underlying dependencies between the current node and its neighbors. The model parameters are treated as the discriminative features to differentiate the spliced images from the natural ones. We apply the model in the block discrete cosine transformation domain and the discrete Meyer wavelet transform domain, and the cross-domain features are treated as the final discriminative features for classification. The support vector machine which is the most popular classifier used in the image-splicing detection is exploited in our paper for classification. To evaluate the performance of the proposed method, all the experiments are conducted on public image-splicing detection evaluation data sets, and the experimental results have shown that the proposed approach outperforms some state-of-the-art methods.

Index Terms—2-D noncausal Markov model, block discrete cosine transformation (BDCT), discrete Meyer wavelet transform, passive image-splicing detection.

I. Introduction

WITH the development of the digital image processing technology and the popularity of digital cameras, tampered images are flooded in our daily life. Some image-tampering processes are harmless; for example, image contrast adjustment, skin smoothing, and white balancing. However, tampered images (especially the spliced images) with malicious purposes could lead to adverse social effects. To regain trust on digital images, many researchers have proposed various approaches to authenticate image data. These approaches can be roughly divided into two main categories: active methods [1]–[4] and passive methods [5]–[23]. The active methods (e.g., digital watermarking and digital signature) try to verify the authenticity of images by checking

whether the previous embedded watermark or digital signature has been destroyed. This kind of approaches can detect image tampering and locate the manipulated regions effectively; however, certain watermarks or signatures have to be inserted into the digital image in the imaging process, which is impractical for most of the commercial cameras. In contrast, the passive methods do not require any prior information and thus they are more suitable for detecting image forgeries on the Internet. The passive methods try to detect image forgeries under the assumption that image tampering would change the underlying statistical characteristics of the original images. The inconsistence of the statistical characteristics is therefore treated as the evidences for image-tampering detection. Among all kinds of image-tampering operations, splicing is the most fundamental and essential operation in creating image forgeries [7]. Hence image-splicing detection is of vital importance in digital image forensics. In this paper, we focus our research on the passive image-splicing detection method.

In recent years, various kinds of passive image-splicing detection approaches have been proposed. Shi *et al.* [15] proposed a natural image model for image-splicing detection. They treated the neighboring differences of block discrete cosine transformation (BDCT) coefficients of an image as a (1-D) signal. The dependencies between neighboring nodes (or rounded BDCT coefficients) along certain direction (horizontal or vertical) were modeled as a causal Markov model and the transition probability matrix, which was regarded as a discriminative feature vector for support vector machine (SVM) classification. Wang *et al.* [16] proposed a gray co-occurrence matrix-based method to detect image splicing. The adjacent difference array of pixel intensities was modeled as 1-D signal and the second-order statistics, that is, gray co-occurrence matrix, were extracted as discriminative features for classification. Sutthiwan *et al.* [17], [18] and Wang *et al.* [19] introduced the causal Markov model, respectively, in the BDCT domain and spatial domain to detect image tampering in chroma channels, and their experiments have shown that the detection rate over CASIA data set can achieve as high as 99%. However, Patchara *et al.* [20] have verified that the high detection rate in [17]–[19] may be related to the artifacts introduced by the postprocessing (double JPEG compressions) in CASIA. Patchara *et al.* [20] rectified the CASIA data set and the experimental results showed that the detection rate of the causal Markov model-based features was reduced to 78% on the rectified data set. Pevný *et al.* [21] proposed
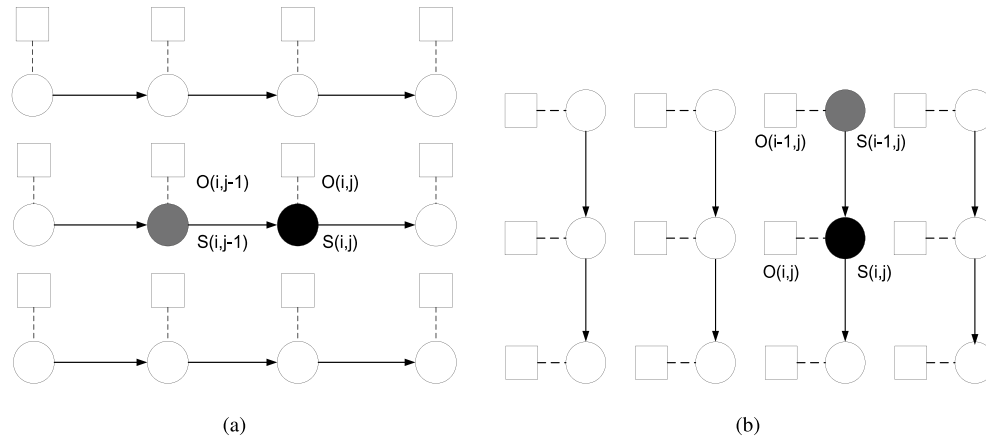
Fig. 1.   Classical 1-D Markov model used in image splicing. Circles: states. Squares: observations corresponding to the states. (a) Horizontal direction. (b) Vertical direction.

subtractive pixel adjacency matrix (SPAM)-based features for steganalysis; they model SPAM as a Markov process and the second-order Markov transition probability matrices along different directions (i.e., $\rightarrow, \leftarrow, \downarrow, \uparrow, \searrow, \nwarrow, \swarrow, \nearrow$) are treated as features for SVM prediction. Kirchner and Fridrich [22] extended the SPAM features to detect median filtering of JPEG compressed images, and experimental results proved that SPAM can be treated as a general-purpose detector for image-tampering detection. Recently, He *et al.* [23] introduced the causal Markov model to both Discrete Cosine Transformation (DCT) and DWT domains and detected the image splicing by the cross-domain Markov features.

Among all the statistical features for image-splicing detection, the Markov-based features [15], [17]–[23] have been demonstrated to be one of the most effective features. The traditional approaches based on the Markov model usually treated the image as 1-D signal and captured the dependency between current node and its previous node along certain direction. However, as an image is a 2-D signal in nature, each element in an image is usually related with its surrounding neighbors in all directions. The simplified Markov model used in the traditional approaches may not depict the image characteristics sufficiently. To solve this problem, a noncausal Markov model has been proposed in this paper which treats the image as a 2-D signal and the dependencies between the current node and its neighbors in all directions are considered. Because there is no analytic solution to the 2-D noncausal model, we split the noncausal model into several 2-D causal models and analyze these models sequentially to approximate the 2-D noncausal model. The 2-D causal submodels can be depicted by the state transition probability matrix, probability density function of each state, and the prior probability of each state. The transition probability matrix depicts the statistical dependency characteristics among neighboring nodes in the model. The probability density function describes the distribution of the observations of each state. The prior probability calculates the frequency of occurrences of each state. Because the proposed feature vector is usually of high dimensionality, SVM is employed as the classifier to overcome the possible overfitting problem. The experimental results demonstrate that

the proposed 2-D noncausal Markov model could effectively differentiate the spliced images from the authentic ones over the public data set [24] and the detection rates of proposed features outperforms the state-of-the-art approaches.

The rest of this paper is organized as follows. The proposed 2-D noncausal Markov model and its solution are introduced in Section II. Image-splicing detection using the proposed 2-D noncausal Markov model is described in Section III. Section IV presents the experimental results of the proposed approach compared with those of several state-of-the-art methods. Discussions on these experimental results are also given in this section. Finally, Section V draws the conclusion.

II. 2-D NONCAUSAL MARKOV MODEL AND ITS SOLUTION

The classical 1-D Markov model depicts the state dependences in the 1-D sense along certain direction which is shown in Fig. 1. It is observed from the figure that the current state (denoted by the black filled circle) is only dependent on its previous state (denoted by the gray filled circle). However, image is a 2-D signal in natural and each state in an image is affected by its surrounding states (nodes). Generalization of the classical 1-D Markov model to represent the state dependencies from surrounding neighbors in all directions leads to a generalized 2-D noncausal model [25] as shown in Fig. 2(a). Although the generalized noncausal model could depict as much underlying information as possible, it is computationally infeasible. In this paper, we simplify the generalized noncausal model to reduce the computational complexity and only consider the nearest four neighbors' noncausal dependencies, which deduces a 2-D noncausal Markov model as shown in Fig. 2(b).

A. 2-D Noncausal Markov Model

Ma *et al.* [26] gives the definition of a noncausal multidimensional hidden Markov model.

1) There are two layers of random variable sets, that is, the hidden states $S = \{S(i, j), i = 1 : M, j = 1 : N\}$ and corresponding observations $O = \{O(i, j), i = 1 : M, j = 1 : N\}$. The hidden state variable nodes $S(i, j)$ lay on a 2-D grid where the relative positions of nodes reflex
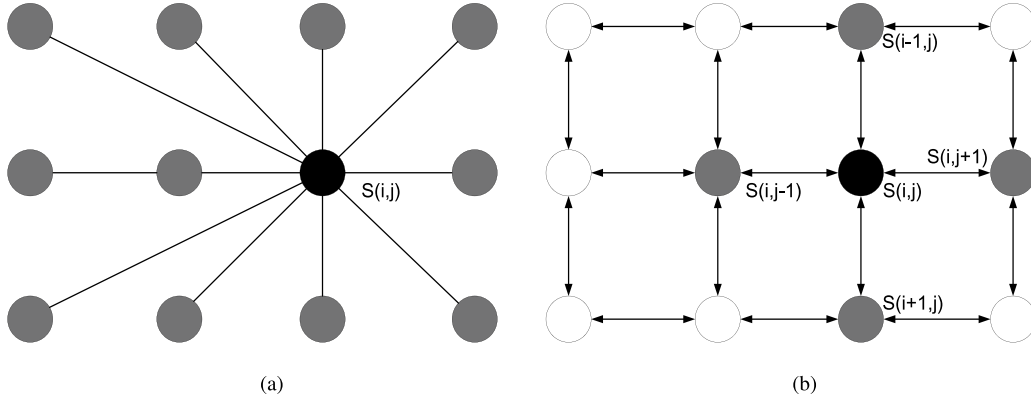
Fig. 2. 2-D noncausal models. (a) Generalized noncausal model. (b) Proposed 2-D noncausal Markov model.

spatial dependencies between them. The hidden states are not observable, but can only be observed through the observations.

2) For each state node $S(i, j)$, its conditional distribution is determined by a set of neighboring nodes that affects it, that is, $P(S(i, j)|S(m, n) \in S, (m, n) \neq (i, j)) = P(S(i, j)|S(m, n) \in N, (m, n) \neq (i, j))$, where in this equation, $N \subset S$ is a set of neighboring nodes of node $S(i, j)$.

In this paper, we propose a 2-D hidden noncausal Markov model which follows the above definitions correspondingly, and it consists of three parts.

1) Let $S = \{s(i, j)|1 \leq i \leq I, 1 \leq j \leq J\}$ and $O = \{o(i, j)|1 \leq i \leq I, 1 \leq j \leq J\}$ be the state set and the observation set, respectively, where i and j are the spatial coordinates, and I and J are the number of rows and columns in the image. Each observation $o(i, j)$ corresponds to the state $s(i, j)$. Observations in the image can be defined according to the practical issues, for example, BDCT coefficient difference array [15], DWT coefficient array [23] or pixel intensity difference array [16], and so forth.

2) Let $P(s(i, j)|N(s(i, j)))$ be the state dependence in the image, where $N(s(i, j))$ is the set of neighboring states that will affect the current state, that is, $s(i, j)$. For a noncausal model, $N(s(i, j))$ consists of the neighboring states from all the directions as shown in Fig. 2(a). Generally speaking, the generalized noncausal model is computationally infeasible; therefore, the markovian process (i.e., the current state only depends on its nearest states) is introduced to reduce the computational complexity. The structure of 2-D noncausal Markov model proposed is shown in Fig. 2(b). In the model, the current state (black filled circle) is affected by its four nearest neighbors (gray filled circles), and the mutual dependences between neighboring nodes are depicted by the double-headed arrows. Specifically, when considering four directional neighbors, the state dependence can be formulated as

$$P(s(i, j)|N(s(i, j)))$$
$$= P(s(i, j)|s(i - 1, j), s(i, j - 1),$$
$$s(i, j + 1), s(i + 1, j)). \quad (1)$$

3) Let Q be the total number of states and thus $s(i, j) \in \{1, 2, \ldots, Q\}$. The distribution of $o(i, j)$ corresponding to state $s(i, j)$ is formulated as $f(o(i, j)|s(i, j))$. If the state set S is unknown, the model would evolve to be a 2-D noncausal hidden Markov [25], [26] model which is computationally expensive. To simplify the problem, we separate the state set into $2q + 1$ levels ($2q + 1 = Q$) according to the distribution of observations. An example is shown in Fig. 3 which gives the distributions of BDCT coefficient difference arrays (horizontal direction and vertical direction) over the data set in [24]. The observations are separated into $2q + 1$ ($q = 5$ in Fig. 3) levels and for a random observation $o(i, j)$

$$s(i, j) = s \text{ if } \{s - 0.5 < o(i, j) < s$$
$$+ 0.5|s \in \{-q, -q + 1, \ldots, q - 1, q\}\}. \quad (2)$$

$f(o(i, j)|s(i, j) = s)$ ($f_s(o(i, j))$ in short) is the probability density function of state s and the formulation of $f_s(o(i, j))$ usually varies according to various applications.

The fundamental three parts in the proposed model satisfy the definitions of the noncausal multidimensional (in 2-D sense) hidden Markov model given in [26]. Two layers, that is, the hidden state set S and the observation set O, are adopted in our model. The state set S lies on the 2-D grid and the relative positions of its nodes reflects the spatial dependencies between them. Hence, our model is in 2-D sense and the preceding definition (1) is satisfied. The state dependencies in our model are given as (1) where $N(s(i, j))$ is the set of nearest neighboring states of current state $s(i, j)$. Hence, our model is noncausal and definition (2) given previously is satisfied.

Although our model is designed according to the definitions of multidimensional noncausal Markov model given in [26], there are mainly two differences between these two models, which makes the proposed model more suitable for image-splicing detection.

1) Ma *et al.* [26] proposed a block-based noncausal Markov model for image segmentation. They split an input image into several nonoverlapping small blocks with the same sizes, and each block corresponds to a state. Although
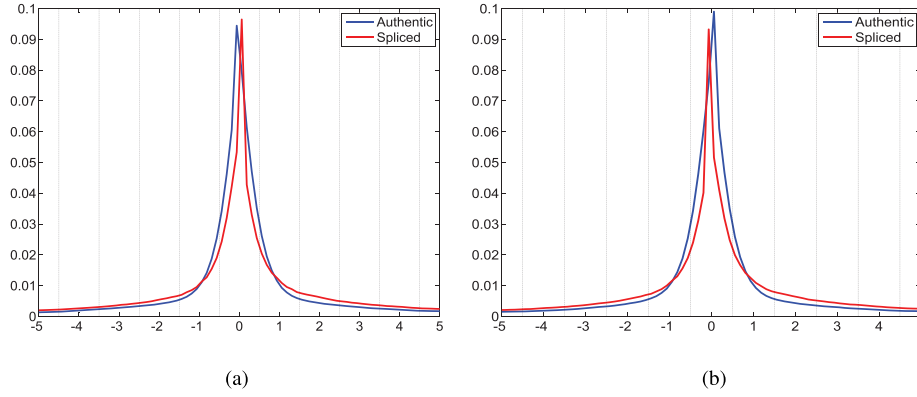
Fig. 3.   Distributions of the BDCT coefficient difference arrays over data set [24]. (a) Horizontal difference array. (b) Vertical difference array.

the block-based noncausal Markov model has been proved to be an effective tool for image content-based classification (which mainly focus on the low-frequency information [25], [26]), directly applying it to image-splicing detection (which tries to expose the splicing artifacts from the high-frequency information [6], [7], [15]) is not appropriate. For the block-based model, the high-frequency coefficients in a block tend to be overwhelmed by the low-frequency coefficients, which would lead to performance degradation for splicing detection. In this paper, we apply the 2-D noncausal Markov model on the transformed domains (which would be introduced in Section III), and each coefficient in the 2-D array corresponds to an observation (state). Hence, the splicing artifacts reflected by the high-frequency coefficients could be captured by this elementwise 2-D noncausal Markov model.

2) The second difference is the way how to establish the state sequence. In [26], an iterative algorithm based on a general forward-backward (GFB) algorithm was proposed to estimate the state sequence. For a state sequence with length $w(u)$, the GFB algorithm needs to calculate $M^{w(u)}$ (M is the number of states) possible subset-state sequences. GFB algorithm is computationally infeasible for the elementwise 2-D noncausal Markov model, because the length $w(u)$ of the state sequence is too long to handle. To avoid the $M^{w(u)}$ order of magnitudes calculations involved in the GFB algorithm, we adopt the rule of (2) in the manuscript to estimate the state sequences and simplify the calculation. Therefore, the proposed model could capture the noncausal statistical characteristics in an efficient manner.

B. Solution to 2-D Noncausal Markov Model

Because there is no analytic approach to the noncausal Markov model, we would have to reformulate and simplify the problem first. Inspired by [26], we first divide the noncausal Markov model into several causal 2-D Markov models which are analytically solvable, then solve these causal submodels simultaneously to obtain a feasible solution to the noncausal Markov model. The 2-D noncausal Markov model shown in

Fig. 2(b) can be split into a series of causal submodels by the following steps as shown in Fig. 4.

1) Input the observation 2-D array, get the noncausal state dependency topology and identify the noncausal state dependencies which are denoted by double-headed arrows.
2) Each noncausal dependency between neighboring states along certain direction (e.g., horizontal, vertical) is decomposed into a couple of causal dependencies (i.e., $\{\rightarrow, \leftarrow\}$, $\{\uparrow, \downarrow\}$) while preserving dependencies from other directions unchanged.
3) Repeat step 2) until all the noncausal state dependences (double-headed arrows) are replaced by causal state dependences (single-headed arrows). Finally, we can get the causal state-dependency graphs.

For an arbitrary noncausal model, the number of decomposed causal models is 2^M where M is the number of bidirectional state dependencies in the model. In this paper, only the state dependencies along vertical and horizontal directions are considered, and thus the 2-D noncausal Markov model is decomposed into four causal submodels (the decomposition procedure is shown in Fig. 4). In the decomposition procedure, the state dependencies information is well preserved. Furthermore, each causal model keeps the state dependencies along certain direction and all the submodels are correlated with each other. Therefore, the framework is not simply a collection of uncorrelated causal models but a precise representation of the original 2-D noncausal model.

After decomposing the noncausal Markov structure into four causal submodels, we solve each submodel, respectively, and obtain the submodel parameters. The 2-D causal Markov submodel is formulated by the following three fundamental parts, which can be denoted as $\{\boldsymbol{\pi}, \boldsymbol{A}, \boldsymbol{B}\}$.

1) $\boldsymbol{\pi}$ is the initial probability vector for all the states, that is, $\boldsymbol{\pi} = \{\pi_1, \pi_2, \ldots, \pi_Q\}$, where

$$\pi_s = P(s(i, j) = s), \quad 1 \leq i \leq I, \quad 1 \leq j \leq J,$$
$$s \in \{1, 2, \ldots, Q\}.$$

2) $\boldsymbol{A}$ is the transition probability matrix, which is formulated as

$$\boldsymbol{A} = \left\{ a_{uvw}^k | u, v, w \in \{1, 2, \ldots, Q\}, k \in \{1, 2, 3, 4\} \right\}$$
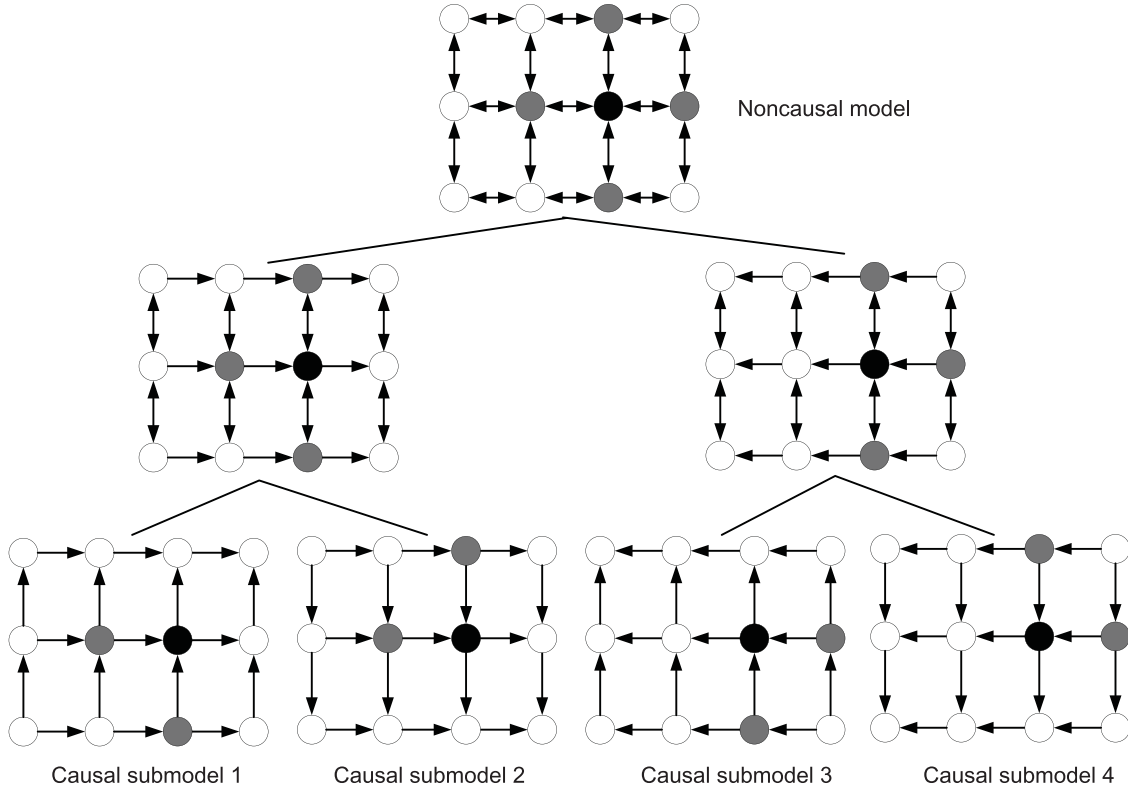
Fig. 4. Decomposition procedure of 2-D noncausal Markov model into four 2-D causal Markov submodels.

where a_{uvw}^k is the transition probability from the previous state set (v, w) to the current state u in the kth causal model

$$
\begin{aligned}
a_{uvw}^k &= P(s(i, j) = u | N^k(s(i, j)) = (v, w)) \\
&= \frac{\sum_i \sum_j \delta(s(i, j) = u, N^k(s(i, j)) = (v, w))}{\sum_i \sum_j \delta(N^k(s(i, j)) = (v, w))}
\end{aligned}
\tag{3}
$$

where $\delta(\cdot)$ is the delta function (1 for truth and 0 for false), $N^k(s(i, j))$ is an ordered set of nearest neighbors of $s(i, j)$ in the kth causal model and is given as

$$
N^k(s(i, j)) = \begin{cases}
(s(i + 1, j), s(i, j - 1)), & k = 1 \\
(s(i - 1, j), s(i, j - 1)), & k = 2 \\
(s(i + 1, j), s(i, j + 1)), & k = 3 \\
(s(i - 1, j), s(i, j + 1)), & k = 4.
\end{cases}
\tag{4}
$$

From (3) and (4), it can be observed that $a_{uvw}^k \geq 0$ and $\sum_{u=1}^Q a_{uvw}^k = 1$. Different from that for 1-D signals, the transition probability for 2-D signals is a third-order statistics that reflects the state dependencies between the current state and the two neighboring states. Hence, the dimension of transition probability matrix of each causal submodel is Q^3.

3) $\boldsymbol{B}$ is the parameter set for the probability density function $f_s(o(i, j))$. The formulation of the probability density function usually depends on the distribution

of the observations and the underlying data structure. In our application of image-splicing detection, to remove the influence caused by image contents, the differences between adjacent pixels or nodes in spatial and frequency domain are usually adopted as observations. As shown in Fig. 3, the distributions of the observations usually have an impulse-like shape, and thus a mixture model is applied to $f_s(o(i, j))$ and the formulation of $f_s(o(i, j))$ is given as

$$
f_s(o(i, j)) = \begin{cases}
\sum_{l=1}^L P_s^l e^{-\frac{(o(i,j) - \mu_l)^2}{2\sigma_l^2}}, & s = 0 \\
\sum_{l=1}^L P_s^l \lambda_s^l e^{-\lambda_s^l(o(i,j) - s + 0.5)}, & s \neq 0
\end{cases}
\tag{5}
$$

where P_s^l ($\sum_{l=1}^L P_s^l = 1$, $P_s^l \geq 0$) is the prior probability (or weighting) of the lth component for state s, μ_l and σ_l are, respectively, the mean and standard deviation of the lth Gaussian mixture, and λ_s^l is the parameter of the lth component exponential function for state s. $f_s(o(i, j))$ is modeled as L-component Gaussian mixture model for state 0 and L-component exponential mixture model for state $s \neq 0$ according to the distribution shown in Fig. 3. Therefore, the parameter set $\boldsymbol{B}$ is composed of all the parameters of the two kinds of mixture models and is given as

$$
\boldsymbol{B} = \big\{ P_s^l, \mu_l, \sigma_l, \lambda_s^l \big| s \in \{-q, -q + 1, \ldots, q - 1, q\}, \\
l \in \{1, 2, \ldots, L\} \big\}.
$$

All the parameters in $\boldsymbol{B}$ can be obtained via an EM algorithm [27]. The EM algorithm tries to maximize the expectation of the log-likelihood function iteratively which is determined by the observations and the current estimates of parameters. Assuming the observations are mutually independent, the log-likelihood function can be expressed as

$$\mathcal{L}(\boldsymbol{\theta}_s) = \sum_i \sum_j \ln\big(f_s(o(i,j)|l;\boldsymbol{\theta}_s)P_s^l\big)$$
$$\times \delta(s - 0.5 < o(i,j) < s + 0.5)$$
$$= \sum_{i'} \sum_{j'} \ln\big(f_s(o(i',j')|l;\boldsymbol{\theta}_s)P_s^l\big)$$

where $(i', j') = \{(i,j)|s - 0.5 < o(i,j) < s + 0.5\}$, $\boldsymbol{\theta}_s$ is the parameter set of the probability density function of state s. Let $\boldsymbol{P}_s = [P_s^1, P_s^2, \ldots, P_s^L]^T$ the unknown parameter vector $\boldsymbol{\Theta}_s = [\boldsymbol{\theta}_s, \boldsymbol{P}_s]^T$. Two steps are involved to estimate the unknown parameters.

1) *E-Step:* Calculate the expectation of log-likelihood function

$$E(\mathcal{L}(\boldsymbol{\theta}_s)) = E\left(\sum_{i'}\sum_{j'}\ln\big(f_s(o(i',j')|l;\boldsymbol{\theta}_s)P_s^l\big)\right)$$
$$= \sum_{i'}\sum_{j'}\sum_{l}^{L} P(l|o(i',j');\boldsymbol{\Theta}_s)$$
$$\times \ln\big(f_s(o(i',j')|l;\boldsymbol{\theta}_s)P_s^l\big).$$

2) *M-Step:* Maximize the log-likelihood with respect to $\boldsymbol{\theta}_s$ and P_s^l and update the parameter set for the $(t + 1)$th iteration by (6)–(9). Note that $\boldsymbol{\theta}_s = \{\mu_l, \sigma_l | l \in \{1, 2, \ldots, L\}\}$ if $s = 0$, else $\boldsymbol{\theta}_s = \{\lambda_s^l | l \in \{1, 2, \ldots, L\}\}$

$$\mu_s^l(t+1) = \frac{\sum_{i'}\sum_{j'} P(l|o(i',j');\boldsymbol{\Theta}_s(t))o(i',j')}{\sum_{i'}\sum_{j'} P(l|o(i',j');\boldsymbol{\Theta}_s(t))} \quad (6)$$

$$\sigma_s^l(t+1)$$
$$= \frac{\sum_{i'}\sum_{j'} P(l|o(i',j');\boldsymbol{\Theta}_s(t))\|o(i',j') - \mu_s^l(t+1)\|^2}{\sum_{i'}\sum_{j'} P(l|o(i',j');\boldsymbol{\Theta}_s(t))}$$
$$(7)$$

$$\lambda_s^l(t+1)$$
$$= \frac{\sum_{i'}\sum_{j'} P(l|o(i',j');\boldsymbol{\Theta}_s(t))}{\sum_{i'}\sum_{j'} P(l|o(i',j');\boldsymbol{\Theta}_s(t))(o(i',j') - s + 0.5)} \quad (8)$$

$$P_s^l(t+1) = \frac{1}{I' \times J'} \sum_{i'}\sum_{j'} P(l|o(i',j');\boldsymbol{\Theta}_s(t)) \quad (9)$$

where I' and J' are the maximum values of i' and j', $P(l|o(i',j');\boldsymbol{\Theta}_s(t))$ is a posterior probability and it can

be derived by

$$P(l|o(i',j');\boldsymbol{\Theta}_s t) = \frac{f_s(o(i',j')|l;\boldsymbol{\theta}_s(t))P_s^l(t)}{\sum_{l=1}^{L} f_s(o(i',j')|l;\boldsymbol{\theta}_s(t))P_s^l(t)}.$$

The EM algorithm starts with a preset initial value and terminates when the estimation error is less than a preset small value.

In summary, we propose an image-splicing-detection specific 2-D noncausal Markov model. During the model optimization stage, the proposed noncausal Markov model is decomposed into four 2-D strictly causal submodels which have analytic solutions, and then these submodels are solved collaboratively to derive an approximate solution to the 2-D noncausal Markov model. The observations are conditionally memoryless and the state transition is first-order Markovian in 2-D sense. It should be noted that since each 2-D causal submodel keeps the state dependencies along certain 2-D direction and all the submodels are correlated with each other, the mutual dependencies of states in the noncausal model are well preserved. Hence, compared with the traditional 1-D Markov model, the proposed model contains much more information about the underlying image characteristics and could better detect image splicing.

III. IMAGE-SPLICING DETECTION BY THE PROPOSED MODEL

The proposed detection method consists of two parts: feature extraction and classification. The 2-D noncausal Markov model-based features are extracted from the source arrays, and then the extracted features are fed into SVM to determine whether the target image has been spliced or not.

A. Feature Extraction

As we known, image splicing would introduce specific statistical artifacts in BDCT domain [15], [20] and DWT domain [5], [15], [23]. In this paper, to verify the effectiveness and generalization ability of the proposed model, we model the adjacent coefficient difference array in the above two different domains as observations for the 2-D noncausal Markov model.

1) BDCT Domain Features: DCT presents good information-packing properties and in image processing, most image content-related information is usually contained in a few low-frequency DCT coefficients. Neglecting these low-frequency coefficients could put emphasis on some content-irrelevant traces caused by image tampering. For most of the spliced images, the region containing tampering traces is usually much smaller than the whole image. Hence, the block DCT transform, which focuses more on the local information, is adopted in image-splicing detection. In our paper, the block size of the BDCT transform is set to $r \times r (r = 2, 4, 8, 16)$ empirically which is sensitive to the splicing operation [15]. The dependences among intrablock BDCT coefficients [15] and interblock BDCT coefficients [23] are employed by the proposed model. For a $r \times r$ BDCT transform, the entire image is divided into a number of
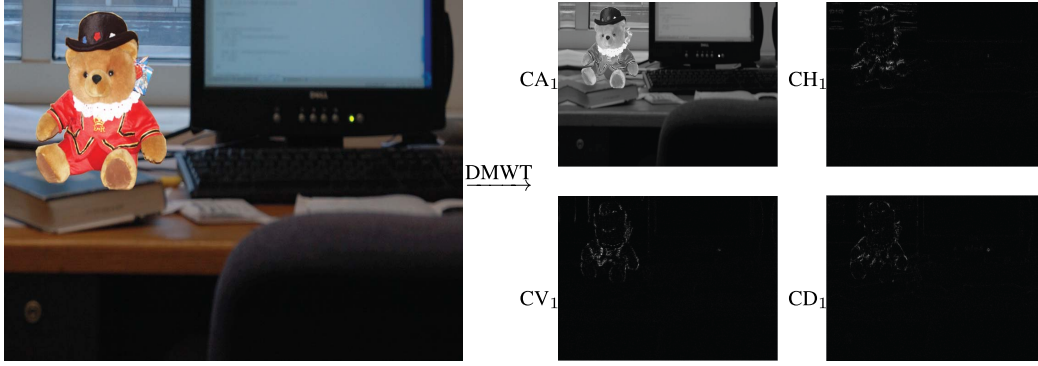
Fig. 5. First-level discrete Meyer wavelet decomposition.

nonoverlapping $r \times r$ blocks and the BDCT array denoted as D can be represented as

$$D = \begin{bmatrix} D_{1,1} & D_{1,2} & \ldots & D_{1,N} \\ D_{2,1} & D_{2,2} & \ldots & D_{2,N} \\ \vdots & \vdots & \ldots & \vdots \\ D_{M,1} & D_{M,2} & \ldots & D_{M,N} \end{bmatrix}$$

where $D_{m,n}(1 \leq m \leq M, 1 \leq n \leq N)$ is a $r \times r$ DCT coefficient array. After the BDCT coefficients array has been computed, we can get four observation sets for the 2-D noncausal Markov model by

$$O_x^h = |D| \otimes h_x, \quad O_x^v = |D| \otimes h_x^T \quad (10)$$

where subscript $x \in \{\text{intra}, \text{inter}\}$, $| \cdot |$ is an elementwise absolute value operator and $\otimes$ is the convolution operation. $h_{\text{intra}} = [-1, 1]^T$ and $h_{\text{inter}} = [-1, 0, 0, 0, 0, 0, 0, 0, 1]^T$ are the filters for $|D|$. O_{intra}^h and O_{intra}^v are the intrablock adjacent difference arrays along horizontal and vertical directions; O_{inter}^h and O_{inter}^v are the interblock adjacent difference arrays along horizontal and vertical directions. O_{intra}^h and O_{intra}^v could capture the correlations in the intrablock coefficients, while the correlations caused by the $r \times r$ blocking artifacts are ignored. Hence, we also consider the correlations between adjacent blocks, that is, O_{inter}^h and O_{inter}^v.

Coefficients in the intrablock and interblock adjacent difference arrays (both horizontal and vertical) are treated as the observations and the relationship between the state and the observations can be formulated as

$$S_x^h = \{ S_x^h(i, j) = s | s - 0.5 < O_x^h(i, j) < s + 0.5, \\ 1 \leq i \leq I, 1 \leq j \leq J \}$$
$$S_x^v = \{ S_x^v(i, j) = s | s - 0.5 < O_x^v(i, j) < s + 0.5, \\ 1 \leq i \leq I, 1 \leq j \leq J \}. \quad (11)$$

After we get the observation sets and the corresponding state sets, the 2-D noncausal Markov model in BDCT domain with the structure shown in Fig. 2(b) can be established, and it can be decomposed into four causal submodels as shown in Fig. 4. Finally, we can solve the causal models sequentially and the parameters of each submodels, that is, $\{\boldsymbol{\pi}, \boldsymbol{A}_i, \boldsymbol{B} | 1 \leq i \leq 4\}$, are extracted as discriminative features for classification. As we get four observation sets, there are total 4×4 causal

submodels and the dimensionality of proposed features is

$$4(4Q^3 + 2(Q-1)L + 3L + Q) = 16Q^3 + 8QL + 4L + 4Q$$

where Q is the number of states and L is the number of components in the mixture model.

2) DWT Domain Features: Discrete wavelet decomposition has been proved as a useful tool for image-tampering detection in the past few years [5], [7], [23]. He *et al.* [23] introduced three-level DMWT for splicing detection and the dependencies of DMWT coefficients across positions, levels, and orientations were modeled as 82 traditional Markov transition probability matrices for classification. Image splicing would introduce abrupt changes in an image, which can be reflected by the high-frequency wavelet subbands (detail coefficients array) [7]. According to [7] and [23], we only apply one-level DMWT on the source images and the detail coefficient arrays at three orientations, that is, horizontal CH_1, vertical CV_1, and diagonal CD_1 are treated as the observation arrays for the proposed noncausal Markov model. CH_1, CV_1, and CD_1 could capture the abrupt changes in different directions which is suitable for detecting splicing signal in the background of image contents [16]. Multilevel wavelet decomposition would introduce more information for classification; however, it also introduce excessive redundant information which could probably confuse the classifier and degrade the detection performance. In Section IV, we will analyze the impact of decomposition levels of DMWT on the image-splicing detection performance.

An illustration for DMWT is shown in Fig. 5. An image in which the teddy bear is the spliced part is shown in the left part of Fig. 5 and its DMWT subbands, that is, CA_1, CH_1, CV_1 and CD_1, are given in the right part. We crop the teddy bear from an authentic image and paste it into a background image by Photoshop CS5 without postprocessing. Note that since the coefficients in the high-frequency subbands are small, we linearly map these high-frequency coefficients to the range of [0, 255] to increase image contrast for better visual effect. It can be observed from Fig. 5 that much of the image background is removed in the high-frequency subbands, and the spliced details are emphasized. Image-splicing detection can be deemed as detecting weak signal (splicing artifacts) in the background of strong noise (image contents) [16], therefore, compared with the approximation array CA_1, the
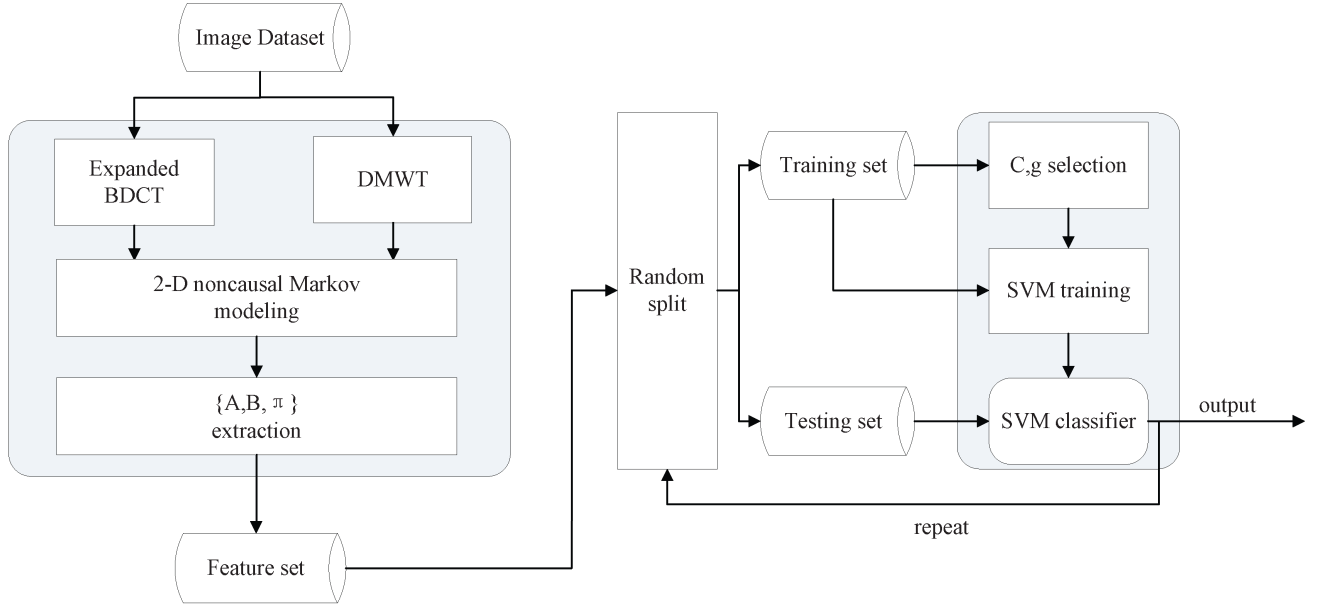
Fig. 6. Framework of the proposed detection method.

high-frequency DMWT subbands are more suitable for image-splicing detection.

After the decomposition of the CH_1, CV_1 and CD_1 subbands, the observation arrays for the 2-D noncausal Markov are modeled by

$$O^h_{\text{subband}} = |\text{subband}| \otimes h_1, \quad O^v_{\text{subband}} = |\text{subband}| \otimes h_1^T \quad (12)$$

where subband $\in \{CH_1, CV_1, CD_1\}$. $O^h_{CH_1}$, $O^v_{CH_1}$ are the adjacent difference arrays along horizontal and vertical directions of the absolute value of CH_1; the definitions of $O^h_{CV_1}$, $O^v_{CV_1}$, $O^h_{CD_1}$, and $O^v_{CD_1}$ are similar to those of $O^h_{CH_1}$ and $O^v_{CH_1}$. After the observation arrays are obtained, the corresponding state arrays can be derived by

$$S^h_{\text{subband}} = \{S^h_{\text{subband}}(i, j) = s \mid s - 0.5 < O^h_{\text{subband}}(i, j) < s + 0.5,$$
$$1 \le i \le I, 1 \le j \le J\}$$
$$S^v_{\text{subband}} = \{S^v_{\text{subband}}(i, j) = s \mid s - 0.5 < O^v_{\text{subband}}(i, j) < s + 0.5,$$
$$1 \le i \le I, 1 \le j \le J\}.$$
$$(13)$$

Finally, we can establish the 2-D noncausal Markov model by the method given in Section II-A and get the model parameters (i.e., discriminative features) by the solution scheme introduced in Section II-B. As six observation sets are obtained, there are 24 causal submodels in total and the dimensionality of the proposed features is

$$6(4Q^3 + 2(Q - 1)L + 3L + Q) = 24Q^3 + 12QL + 6L + 6Q.$$

B. Classification and Framework of the Proposed Method

In our approach, the image-splicing detection is treated as a binary classification problem, that is, the extracted feature vector is fed into a classifier to predict whether it is spliced or not. Hence, the selection of classifier is important and a properly chosen classifier would greatly improve the detection accuracy. In this paper, SVM [28] is adopted to evaluate the

effectiveness of the proposed features for its robustness to overfitting problem. LIBSVM [29] which is a library for SVM is used in our classification work and the radial basis function is selected as the kernel of SVM. Because SVM is a supervised machine learning method, we randomly split the entire feature set extracted into two sets: one for training and the other for testing. The training set is employed to find the optimal hyperplane for classification, and the testing set is used to test the effectiveness of the proposed features.

To handle high-dimensional features and reduce the time complexity, we introduce a distributed scheme to solve the proposed model synchronously. Two clients with six CPU cores are involved in the distributed scheme. A distributed scheme is adopted which can process all the submodels synchronously and reduce the processing time greatly in feature extraction, SVM training, and prediction. Details are given as follows. First, the causal Markov submodels are distributed to different clients (or CPU cores), so the features (or submodel parameters) could be extracted simultaneously. Second, we also conduct SVM parameter selection [i.e., (C, g) selection] on the distributed 2-D grid, that is split the (C, g) 2-D grid into several small 2-D grids which are then distributed to different CPU cores, and all the cores run the parameter-selection algorithm on their small grid synchronously. Third, the distributed scheme has also been introduced in the classifier predictions, since many rounds of experiments are involved to get the average detection accuracy, distributed predictions would greatly reduce the time cost. The detection framework of proposed method is shown in Fig. 6, and the details are given as follows.

1) For a given image, transform it to the BDCT domain and DMWT domain, respectively.
2) Get the observation arrays and state arrays via (10), (11), (12), and (13). Construct 2-D noncausal Markov models for these arrays using the method described in Section II-A.

Fig. 7. Some example images in the DVMM data set [24].

3) Split the noncausal model into four causal submodels by the method proposed in Section II-B, distribute these submodels to the clients, one to each core by the scheduler.

4) Extract the parameter set $\{\boldsymbol{\pi}, \boldsymbol{A}, \boldsymbol{B}\}$ according to the method proposed in Section II-B synchronously on each core, and update the feature vector according to the output of each submodel.

5) Repeat the procedure 1)–4) to get all the feature vectors in the image data set and group all of them into a feature set.

6) Randomly split the feature set into training and testing set proportionally (e.g., 5/6 for training and 1/6 for testing).

7) Conduct SVM parameter selection (i.e., (C, g) selection [30]) on the distributed 2-D grid. That is split the (C, g) 2-D grid into several small 2-D grids which are then distributed to different cores. All the cores run the parameter-selection algorithm on their small grid synchronously, and optimal parameters can be derived by comparing the suboptimal parameters on all the small grid.

8) Input the optimal parameter set (C, g) into SVM, and get the optimal hyperplane of training samples by the training algorithm.

9) Fed feature vectors in the testing set into the trained SVM in 8) and thus the detection accuracy can be obtained.

10) Repeat the steps 6) and 9) several times (e.g., 30) and employ the average detection accuracy to evaluate the effectiveness of the extracted feature to reduce the detection performance turbance caused by the various selections of the training set.

IV. Experimental Results and Analysis

In this section, we first introduce the image-spicing evaluation data set used in the experiments. Then performance evaluation of the proposed model with different parameter settings is provided. After that, we give the performance comparisons with several state-of-the-art splicing detection approaches. Finally, some real-image forgeries are introduced to testify the effectiveness of the proposed scheme.

A. Image Data Set for Investigation

The Columbia Image-Splicing Detection Evaluation Data Set (DVMM) [24] is adopted in our experiments. DVMM consists of 933 authentic images and 912 spliced images and it covers a variety of contents (e.g., smooth, textured, arbitrary object boundary and straight boundary, and so on). All the images in the data set are in BMP format with size of 128×128. The image is kept at a reasonable size (128×128) to ensure that sufficient statistical features can be estimated in each block. The spliced images are created from the authentic ones in the data set by crop-and-paste along object boundaries or crop-and-paste of horizontal (or vertical) strips. Some example images are shown in Fig. 7 where the authentic images are given in the first row and the spliced images are shown in the second row.

B. Detection Results and Discussions

We conduct our experiments over the DVMM data set according to the method proposed in Sections II and III. In the classification phase, to reduce the variations caused by different selections of the training samples, 30 random tests have been performed and the mean and standard deviations of the classification results are recorded. In each of the 30 runs, 5/6 authentic images and 5/6 spliced images are randomly selected to find the optimal (C, g) for SVM and to train the SVM. The rest images are used to test the detection results. The detection performance is measured by the following two criterions: 1) the true positive (TP) rate, true negative (TN) rate, and total accuracy (Accuracy) and 2) the value of the area under ROC curve (AUC) [31].

1) Detection Performance by the Proposed Method: We first investigate the impact of the decomposition level of DMWT on the performance of image-splicing detection. Table I presents the detection accuracies of different subbands (subbands combinations) over image data set [24], where the subscript i denotes the level of the DMWT decomposition, standard deviations over 30 random test are given in the brackets. For fairness purpose, we set $Q = 7$ for all the subbands. It can be observed from Table I that the first-level high-frequency subbands combination (i.e., $CH_1 + CV_1 + CD_1$) achieves the highest detection accuracy compared with other subbands or subbands combinations.

TABLE I

IMPACT OF THE DECOMPOSITION LEVEL OF DMWT ON THE DETECTION PERFORMANCE OVER DATA SET [24]

	CH_i	CV_i	CD_i	$CH_i + CV_i + CD_i$	$\sum_i^2(CH_i + CV_i + CD_i)$	$\sum_i^3(CH_i + CV_i + CD_i)$
$i = 1$	76.12% (1.88)	77.17% (2.04)	79.49% (1.48)	84.92% (1.64)		
$i = 2$	65.95% (2.51)	67.68% (2.15)	67.54% (1.93)	71.09% (2.38)	83.89% (1.85)	81.45% (2.35)
$i = 3$	60.35% (3.07)	65.06% (2.28)	59.54% (2.61)	65.47% (2.20)	N/A	

TABLE II

IMPACT OF BLOCK SIZE OF BDCT ON THE DETECTION PERFORMANCE OVER DATA SET [24]

Block size r	Performance evaluation	Expanded BDCT	Expanded BDCT+DMWT
	TP	76.97% (3.22)	83.82% (3.22)
2×2	TN	73.71% (2.97)	84.47% (2.06)
	Accuracy	75.35% (2.01)	84.15% (1.56)
	TP	84.17% (2.69)	85.60% (2.99)
4×4	TN	77.92% (3.34)	86.25% (2.68)
	Accuracy	81.08% (1.42)	85.92% (1.79)
	TP	90.12% (2.22)	92.99% (1.89)
8×8	TN	90.65% (2.37)	93.75% (1.79)
	Accuracy	90.38% (1.39)	93.36% (1.19)
	TP	83.21% (2.62)	89.36% (2.60)
16×16	TN	83.60% (3.03)	90.72% (2.05)
	Accuracy	83.39% (1.91)	90.31% (1.07)

It is also noted that the multilevel subbands combinations [i.e., $\sum_{i=1}^2(CH_i + CV_i + CD_i)$ and $\sum_{i=1}^3(CH_i + CV_i + CD_i)$] could not improve the detection accuracy, and the excessive redundant features involved would even degrade the detection performance. This experiment can be deemed as an evidence to support our claim in Section III-A2). In the following experiments, we only use CH_1, CH_1, and CD_1 for wavelet domain feature extraction.

The impact of block size r in BDCT on the detection performance is shown in Table II, where Expanded BDCT is the features extracted from the observation arrays defined in (10), DMWT is the features extracted from the observation arrays defined in (12), and Expanded BDCT + DMWT is the combined features. For fairness purpose, we set $Q = 7$ for all the block sizes in BDCT. It can be observed in Table II that with the increase of r the detection performance first increases then drops dramatically, and the 8×8 BDCT achieves the best detecting performance among all the block sizes. Hence, the choice of block size in the multisize BDCT is important for the detection work, and in the following experiments we set $r = 8$ for comparisons.

The detection performance of the proposed 2-D noncausal Markov model-based features with different number of states is presented in Table III, and the averaged ROC curves and the corresponding AUCs are shown in Fig. 8. It can be observed from Table III and Fig. 8 as follows.

1) When the number of states increases, the detection performance first increases then converges rapidly and $Q = 7$ is observed to be a good selection which can

provide almost the highest classification accuracy while the computational cost is also acceptable.

2) Both features in the expanded BDCT domain and DMWT domain contain discriminative information for splicing detection and the features in the expanded BDCT domain outperforms those in DMWT domain.

3) The combined features (or cross domain features) outperforms features in either domain which indicates that the features extracted from the two different domains compensate for each other.

2) Comparisons With Other Detection Approaches: To comprehensively evaluate the proposed method, three state-of-the-art image-splicing/tampering detection methods, that is, Shi *et al.* [15], He *et al.* [23], and SPAM [21], [22], are introduced in our experimental work for comparisons. SPAM with 686 features is a spatial approach which has achieved promising detection capability in image steganalysis and median filtering detection during the past few years. We introduce the SPAM method for experimental comparisons is based on [10] which claims that a natural image model based on a set of carefully selected statistical features under the machine learning framework can be used for both steganalysis and splicing detection, and lessons learnt from steganalysis can be applied to splicing detection to boost the detection performance. To guarantee a fair comparison, we also apply the SPAM method in both BDCT domain and DMWT domain, and detection results of the cross domain features with dimensionality 2744 are presented. All the detection methods are conducted over data set [24] using the classification scheme

TABLE III

DETECTION PERFORMANCE OF THE NONCAUSAL MODEL WITH DIFFERENT NUMBER OF STATES OVER DATA SET [24]

| Number of states	Performance evaluation	Expanded BDCT	DMWT	Expanded BDCT+DMWT
	TP	90.01% (2.11)	83.87% (3.63)	91.58% (2.53)
Q=3	TN	88.56% (2.46)	82.52% (3.38)	90.55% (2.93)
	Accuracy	89.28% (1.37)	83.20% (1.95)	91.07% (1.65)
	TP	90.32% (2.48)	84.83% (3.20)	92.31% (1.77)
Q=5	TN	89.80% (2.50)	85.90% (2.97)	93.03% (2.08)
	Accuracy	90.06% (1.86)	85.35% (2.24)	92.66% (1.52)
	TP	90.12% (2.22)	84.29% (2.43)	92.99% (1.89)
Q=7	TN	90.65% (2.37)	85.57% (3.64)	93.75% (1.79)
	Accuracy	90.38% (1.39)	84.92% (1.64)	93.36% (1.19)
	TP	90.02% (2.48)	83.65% (2.85)	91.54% (2.45)
Q=9	TN	91.14% (2.15)	83.79% (2.49)	93.44% (1.99)
	Accuracy	90.57% (1.58)	83.72% (1.65)	92.47% (1.32)
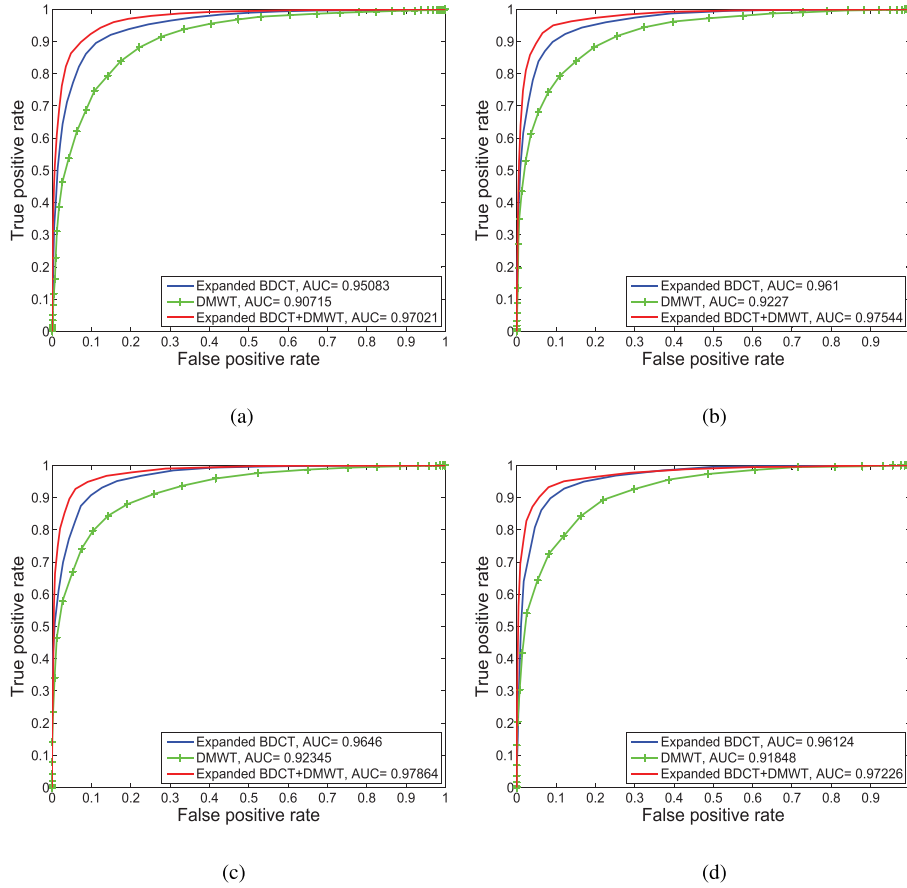
Fig. 8. ROC curves and the corresponding AUCs for expanded BDCT, DMWT, and expanded BDCT + DMWT. (a) $Q = 3$. (b) $Q = 5$. (c) $Q = 7$. (d) $Q = 9$.

described in Section III-B to ensure the fairness and validity. The detection results are given in Table IV and the corresponding ROC curves are shown in Fig. 9. As shown in Table IV, our proposed method ($Q = 7, r = 8$) achieves a detection accuracy as high as 93.36%. Compared with the other three detection methods, the proposed features can achieve at least 2.2% higher average detection accuracy. The dimensionality

of our features is $14\,240$ ($Q = 7, r = 8$), which is higher than the other three detection methods. However, we boost the image-splicing detection rate over 2.2% compared with the state-of-the-art (to our best knowledge) at the cost of higher feature dimensionality.

To comprehensively evaluate the performance of proposed model, we introduce time cost as another indicator

TABLE IV
COMPARISONS WITH OTHER DETECTION METHODS

Method	Shi [15]	He [23]	SPAM [21, 22]	Proposed method (Q=7)
Dimensionality	266	7290	2744	14240
TP	90.01% (2.14)	87.03% (2.02)	89.32% (2.32)	92.99% (1.89)
TN	90.31% (2.29)	88.20% (2.13)	93.04% (2.39)	93.75% (1.79)
Accuracy	90.15% (1.37)	87.61% (1.36)	91.15% (1.55)	93.36% (1.19)

TABLE V
COMPARISONS OF TIME COST

Time cost	Shi [15]	He [23]	SPAM [21, 22]	Proposed
Fea. time	3015.9 s	2072.5 s	3752.7 s	4770.1 s
(C, g) time	58.6 s	2647.6 s	938.1 s	7628.5 s
Pred. time (30 rounds)	23.8 s	747.2 s	241.4 s	1745.1 s
Total time	3098.3 s	5467.3 s	4932.2 s	14143.7 s

for comparisons. Feature extraction time, SVM (C, g) selection time, prediction time over 30 rounds, and the total time are adopted for comparisons. All the schemes are implemented on the same platform, that is, 64-b MATLAB 2013a. The comparison results are presented in Table V, where Fea. time is the feature extraction time, (C, g) time indicates the time cost of (C, g) selection, Pred. time denotes the prediction time over 30 rounds, and Total time equals to the sum of Fea. time, (C, g) time, and Pred. time. For a fair comparison, we first compare the time cost of Shi *et al.* [15], He *et al.* [23], SPAM [21], [22], and the proposed features with state number $Q = 7$ on the same client (Client I) with Intel(R) Core (TM) i7-2600 CPU 3.40 GHz, and the comparison results are presented in Table V. It can be observed in Table V that: 1) Shi [15] is the fastest detection method with the average detection accuracy 90.15% and 2) the proposed method achieves the highest detection accuracy at the cost of the highest time complexity. The dimensionality of the proposed features with $Q = 7$ is 14 240 which is higher than that of the other three methods, and the higher dimensionality inevitably increases the time cost of the detection work.

Then, to verify the effectiveness of the high-dimensional feature-processing scheme introduced in Section III-B, we also calculated the time cost of the proposed features on a distributed system which is composed of Client I and Client II with Intel(R) Duo E7500 CPU 2.93 GHz. The time cost of the distributed noncausal Markov model are listed as follows: Fea. time: 1060.9 s, (C, g) time: 1695.8 s, Pred. time: 388.4 s, and Total time 3145.1 s. Therefore, the high-dimensional feature-processing scheme proposed in Section III-B could dramatically reduce the time cost of the proposed method, and make the proposed high-dimensional features manageable. Because our approach splits a 2-D noncausal model into several causal submodels, it is naturally suitable for the distributed computing. All these submodels are allocated to different CPU cores, and all these cores run the feature extraction algorithm simultaneously, so the distributed scheme could reduce the time cost greatly.
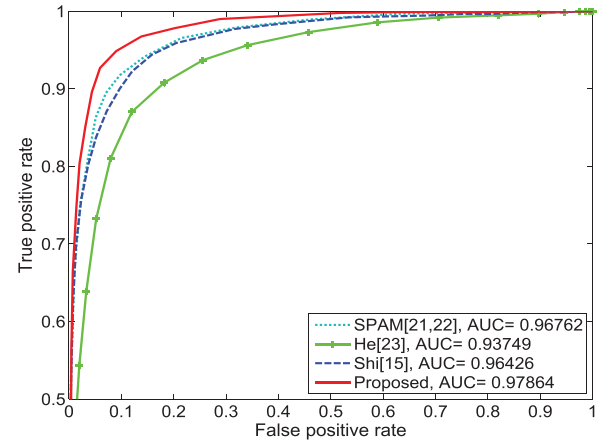

Fig. 9. ROC curves and the corresponding AUCs for different detection methods.

C. Robustness Test

In this section, JPEG compression and median filtering operations are applied on the DVMM data set to test the robustness of the proposed splicing detection method. The JPEG compression level can be measured by the quality factor which is a positive integer in the range [1, 100]. Larger quality factors mean high quality (i.e., less compression) and vice versa. For median filtering, two sizes of filters, that is, 3×3 and 5×5 are used on the data set. After we get the post processed image data set, we conduct experiments according to the procedure shown in Fig. 6. The detection accuracies of the four detection methods are shown in Fig. 10. It can be seen Fig. 10(a) that when the quality factor decreases, the detection accuracies of all the methods decrease. The proposed method with different compression rates always outperforms the other three methods, especially when the quality factors are high. Median filtering also has a negative effect on the detection performance and as it can be seen in Fig. 10(b), the detection accuracies of the proposed method are still higher than that of the other methods.
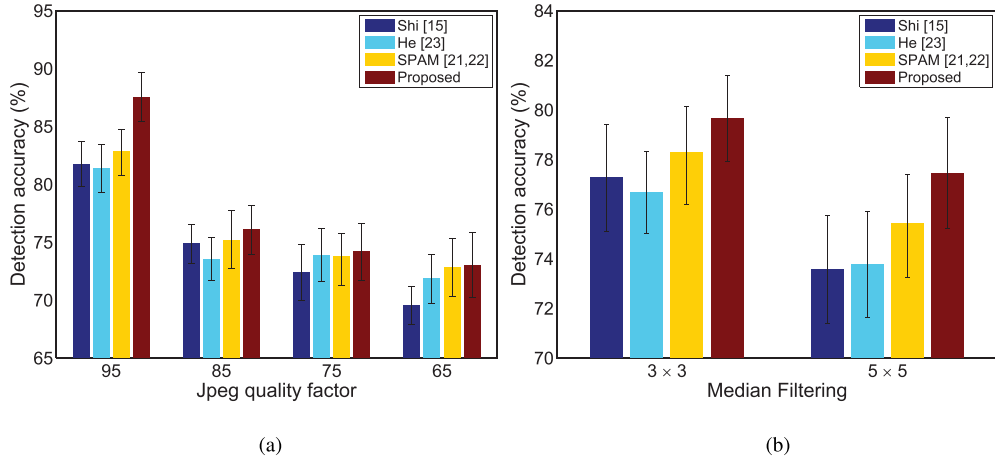
Fig. 10. Robustness comparisons. (a) JPEG compression test. (b) Median filtering test.
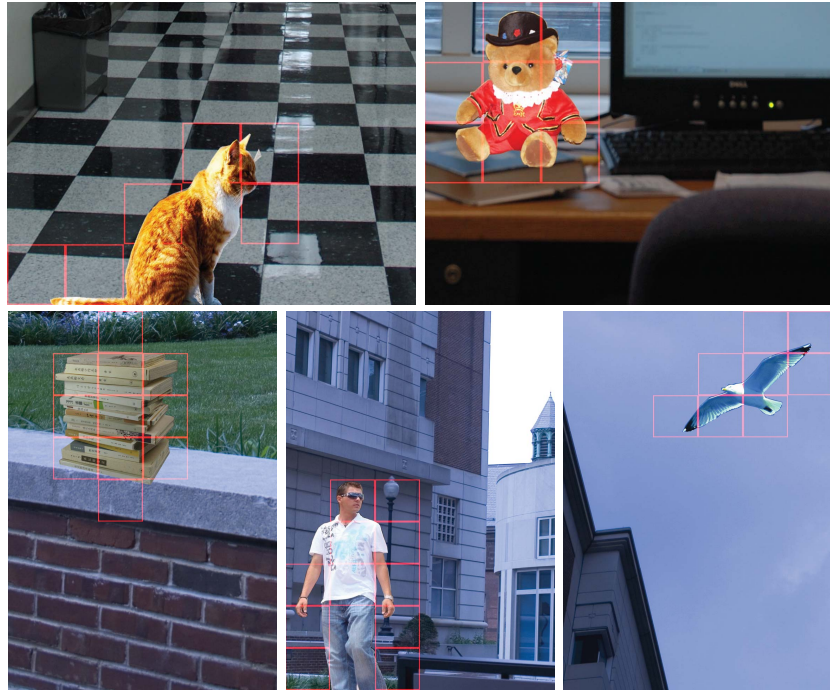

Fig. 11. Detection results of some image forgeries.

D. Splicing Detection on Real-Image Forgeries

To demonstrate the effectiveness of the proposed approach in image forgery detection, we have also generated many image forgeries by the splicing operations for evaluation. The source images are from Columbia Uncompressed Image-Splicing Detection Evaluation Data Set [32] and Uncompressed Color Image Database [33]. We create image forgeries by crop one part of an image and paste it on another image. To eliminate the influence of double JPEG compression and to concentrate on the detection of splicing manipulations, all the source images are uncompressed images with TIFF format, and the image forgeries are also saved as uncompressed TIFF format. For real-image forgery detection, we first train the SVM classifier by the image samples in DVMM data set [24] according to the training framework described in Section III-B, then split the input image as 128×128 nonoverlapping small blocks (since our SVM classifier is trained by 128×128 small images of DVMM data set [24], here we split the image into small blocks with the same size for detection), finally, detect the these small image blocks one by one to get the detection result. Details are given in Algorithm 1, in which G is an image input, ϕ is a trained SVM with fixed parameters, C is a vector to store the position information of manipulated blocks. If the sum of C equals to zero, the input image is authentic, else spliced. We can also get the exact spliced areas by C, because the image is scanned from top to bottom and left to right, there is a unique mapping between c and the spatial position of the image. Finally, all the spliced areas can be labeled according to the spatial locations provided by C. Fig. 11 shows detection results on some real-image forgeries and the spliced areas are highlighted as the indication of image forgeries.

Algorithm 1 Real-Image Forgery Detection by the Proposed Method

Input:
  Unknown image G;
  Trained SVM classifier ϕ;
  $c := 1, C := 0$
Output:
  Label array C
1: Input unknown image G, get its size $[I, J]$;
2: Divide it into $\lfloor \frac{I}{128} \rfloor \times \lfloor \frac{J}{128} \rfloor$ nonoverlapping image blocks;
3: Scan these image blocks from top to bottom and left to right, compute $\{\pi_c, A_c, B_c\}$ of the cth image block G_c;
4: Input $\{\pi_c, A_c, B_c\}$ to the trained SVM ϕ, and get the detection result $\phi(\pi_c, A_c, B_c)$;
5: If $\phi(\pi_c, A_c, B_c) < 0$, update label array $C(c) = 1$;
6: $c := c + 1$, go to step 3 until $c = \lfloor \frac{I}{128} \rfloor \times \lfloor \frac{J}{128} \rfloor$;
7: **return** C.

TABLE VI

DETECTION RESULTS ON IFS-TC DATA SET

	Shi [15]	He [23]	SPAM [21, 22]	Proposed
Score	0.7476	0.7704	0.873	0.901
Pred. time	1.31 s	42.70 s	23.69 s	58.5 s

http://ifc.recod.ic.unicamp.br/fc.website/index.py?sec=09.

E. First IEEE Information Forensics and Security Technical Committee Image Forensics Challenge

The First IEEE Information Forensics and Security Technical Committee (IFS-TC) Image Forensics Challenge [34] is an international competition organized by IFS-TC. IFS-TC published a data set to evaluate the current state-of-the-art techniques with respect to their ability to detect image forgeries. The images in the challenge are captured from different digital cameras with various scenes. All of these images are grouped into two categories: pristine and forged, and the forged images comprise a set of different manipulation techniques such as copy/pasting and splicing. All the pristine and fake images are divided into a training set (1500 images) and a testing set (5713 images). Training set is provided to train a detector (classifier), while the testing set is used to verify the effectiveness of the detector. Detection results of Shi *et al.* [15], He *et al.* [23], SPAM [21], [22], and the proposed method on the testing set are shown in Table VI, where score is a performance indicator that describes the results of classification (high score corresponds to good classification) [34], Pred. time is the predicting time on all the images of the testing set. It can be observed in Table VI that the proposed method get a score 0.901 which is higher than that of the other three methods at the cost of longer prediction time (58.5 s). Although the prediction time of the proposed approach is longer than other methods, the average prediction time is about 0.01 s (i.e., 58.5/5713). And the proposed scheme could detect images in real time. There are a few state-of-the-art algorithms in the IFS-TC challenge perform better than the proposed scheme, and further research would be conducted to improve the detection performance of our method.

V. CONCLUSION

The Markov model has been proved to be one of the most effective tools for image-tampering detection and image steganalysis. To our best knowledge, almost all the image-tampering detection approaches based on the Markov models (in BDCT domain or DWT domain) treated the image as a 1-D causal signal. Hence, the traditional model only depicts the state dependencies between adjacent states along certain directions (e.g., horizontal, vertical). To take more information into consideration, a 2-D noncausal Markov model is proposed in this paper to better model the 2-D image and each state in the proposed model depends on its surrounding states simultaneously. Because there is no direct analytic solution to this model, we decompose the noncausal model into four 2-D causal submodels and solve these submodels sequentially. For each causal submodel, the current state depends on its nearest states in the 2-D sense (2-D dependency or Markovian property for 2-D signals). These causal submodels are described by the prior probabilities of each state, the parameters of probability density function of each state and the state transition probability matrix. All these model parameters are treated as discriminative features for classification. We apply our model in the BDCT domain and DMWT domain, and the model proved its generalization and effectiveness in the two different domains. Experimental results show that the proposed noncausal Markov model outperforms some state-of-the-art methods over two published image-splicing detection evaluation data sets.

REFERENCES

[1] M. M. Yeung, "Digital watermarking," *Commun. ACM*, vol. 41, no. 7, pp. 30–33, Jul. 1998.
[2] C.-Y. Lin and S.-F. Chang, "A robust image authentication method distinguishing JPEG compression from malicious manipulation," *IEEE Trans. Circuits Syst. Video Technol.*, vol. 11, no. 2, pp. 153–168, Feb. 2001.
[3] K. C. Chan, Y. S. Moon, and P. S. Cheng, "Fast fingerprint verification using subregions of fingerprint images," *IEEE Trans. Circuits Syst. Video Technol.*, vol. 14, no. 1, pp. 95–101, Jan. 2004.
[4] H.-H. Tsai and C.-C. Liu, "Wavelet-based image watermarking with visibility range estimation based on HVS and neural networks," *Pattern Recognit.*, vol. 44, no. 4, pp. 751–763, Apr. 2011.
[5] H. Farid and S. Lyu, "Higher-order wavelet statistics and their application to digital forensics," in *Proc. Conf. Comput. Vis. Pattern Recognit. (CVPR) Workshop*, Madison, WA, USA, Jun. 2003, p. 94.
[6] T.-T. Ng, S.-F. Chang, and Q. Sun, "Blind detection of photomontage using higher order statistics," in *Proc. Int. Symp. Circuits Syst. (ISCAS)*, Vancouver, BC, Canada, May 2004, pp. V-688–V-691.
[7] W. Chen, Y. Q. Shi, and W. Su, "Image splicing detection using 2-D phase congruency and statistical moments of characteristic function," in *Proc. SPIE Conf. Secur., Steganogr., Watermarking Multimedia Contents*, San Jose, CA, USA, Jan. 2007, pp. 1–8.

[8] T. C.-I. Lin, M.-K. Chang, and Y.-L. Chen, "A passive-blind forgery detection scheme based on content-adaptive quantization table estimation," *IEEE Trans. Circuits Syst. Video Technol.*, vol. 21, no. 4, pp. 421–434, Apr. 2011.

[9] J. Dong, W. Wang, T. Tan, and Y. Q. Shi, "Run-length and edge statistics based approach for image splicing detection," in *Proc. 7th Int. Workshop Digit. Watermarking (IWDW)*, Busan, Korea, 2009, pp. 76–87.

[10] Y. Q. Shi, C. Chen, G. Xuan, and W. Su, "Steganalysis versus splicing detection," in *Proc. 6th Int. Workshop Digit. Watermarking (IWDW)*, Guangzhou, China, 2008, pp. 158–172.

[11] Z. He, W. Sun, W. Lu, and H. Lu, "Digital image splicing detection based on approximate run length," *Pattern Recognit. Lett.*, vol. 32, no. 12, pp. 1591–1597, Sep. 2011.

[12] P. Kakar, N. Sudha, and W. Ser, "Exposing digital image forgeries by detecting discrepancies in motion blur," *IEEE Trans. Multimedia*, vol. 13, no. 3, pp. 443–452, Jun. 2011.

[13] X. Zhao, J. Li, S. Li, and S. Wang, "Detecting digital image splicing in chroma spaces," in *Proc. 9th Int. Workshop Digit. Watermarking (IWDW)*, Seoul, Korea, 2011, pp. 12–22.

[14] M. K. Johnson and H. Farid, "Exposing digital forgeries in complex lighting environments," *IEEE Trans. Inf. Forensics Security*, vol. 2, no. 3, pp. 450–461, Sep. 2007.

[15] Y. Q. Shi, C. Chen, and W. Chen, "A natural image model approach to splicing detection," in *Proc. 9th Workshop Multimedia Secur. (MM & Sec)*, Dallas, TX, USA, 2007, pp. 51–62.

[16] W. Wang, J. Dong, and T. Tan, "Effective image splicing detection based on image chroma," in *Proc. 16th IEEE Int. Conf. Image Process. (ICIP)*, Cairo, Egypt, Nov. 2009, pp. 1257–1260.

[17] P. Sutthiwan, Y.-Q. Shi, J. Dong, T. Tan, and T.-T. Ng, "New developments in color image tampering detection," in *Proc. IEEE Int. Symp. Circuits Syst. (ISCAS)*, Paris, France, May/Jun. 2010, pp. 3064–3067.

[18] P. Sutthiwan, Y. Q. Shi, W. Su, and T.-T. Ng, "Rake transform and edge statistics for image forgery detection," in *Proc. IEEE Int. Conf. Multimedia Expo (ICME)*, Singapore, Jul. 2010, pp. 1463–1468.

[19] W. Wang, J. Dong, and T. Tan, "Image tampering detection based on stationary distribution of Markov chain," in *Proc. 17th IEEE Int. Conf. Image Process. (ICIP)*, Hong Kong, Sep. 2010, pp. 2101–2104.

[20] S. Patchara, Y. Q. Shi, H. Zhao, T.-T. Ng, and W. Su, "Markovian rake transform for digital image tampering detection," *Trans. Data Hiding Multimedia Secur. VI*, vol. 6730, pp. 1–17, Jul. 2011.

[21] T. Pevny, P. Bas, and J. Fridrich, "Steganalysis by subtractive pixel adjacency matrix," *IEEE Trans. Inf. Forensics Security*, vol. 5, no. 2, pp. 215–224, Jun. 2010.

[22] M. Kirchner and J. Fridrich, "On detection of median filtering in digital images," *Proc. SPIE, Media Forensics Secur. II*, vol. 7541, pp. 754110-1–754110-12, Jan. 2010.

[23] Z. He, W. Lu, W. Sun, and J. Huang, "Digital image splicing detection based on Markov features in DCT and DWT domain," *Pattern Recognit.*, vol. 45, no. 12, pp. 4292–4299, Dec. 2012.

[24] T.-T. Ng, J. Hsu, and S.-F. Chang. *Columbia Image Splicing Detection Evaluation Dataset*. [Online]. Available: http://www.ee.columbia.edu/ln/dvmm/downloads/AuthSplicedDataSet/dlform.html

[25] J. Li, A. Najmi, and R. M. Gray, "Image classification by a two-dimensional hidden Markov model," *IEEE Trans. Signal Process.*, vol. 48, no. 2, pp. 517–533, Feb. 2000.

[26] X. Ma, D. Schonfeld, and A. A. Khokhar, "Video event classification and image segmentation based on noncausal multidimensional hidden Markov models," *IEEE Trans. Image Process.*, vol. 18, no. 6, pp. 1304–1313, Jun. 2009.

[27] A. P. Dempster, N. M. Laird, and D. B. Rubin, "Maximum likelihood from incomplete data via the EM algorithm," *J. Roy. Statist. Soc. B*, vol. 39, no. 1, pp. 1–38, 1977.

[28] V. N. Vapnik, *Statistical Learning Theory*. New York, NY, USA: Wiley, 1998.

[29] C.-C. Chang and C.-J. Lin, "LIBSVM: A library for support vector machines," *ACM Trans. Intell. Syst. Technol.*, vol. 2, no. 3, pp. 1–27, 2011.

[30] C.-W. Hsu, C.-C. Chang, and C.-J. Lin, "A practical guide to support vector classification," Dept. Comput. Sci., Nat. Taiwan Univ., Taipei, Taiwan, Tech. Rep., Apr. 2010. [Online]. Available: http://www.csie.ntu.edu.tw/~cjlin/papers/guide/guide.pdf

[31] T. Fawcett, "ROC graphs: Notes and practical considerations for data mining researchers," HP Labs, Palo Alto, CA, USA, Tech. Rep. HPL-2003-4, 2004.

[32] Y.-F. Hsu and S.-F. Chang, "Detecting image splicing using geometry invariants and camera characteristics consistency," in *Proc. IEEE Int. Conf. Multimedia Expo*, San Jose, CA, USA, Jul. 2006, pp. 549–552.

[33] G. Schaefer and M. Stich, "UCID—An uncompressed colour image database," *Proc. SPIE*, vol. 5307, pp. 472–480, Dec. 2003.

[34] A. R. Rocha, A. Piva, and J. Huang, "The first IFS-TC image forensics challenge," *IEEE Inf. Forensics Security Tech. Committee*, Nov. 2012. [Online]. Available: http://ifc.recod.ic.unicamp.br/fc.website/index.py

Xudong Zhao (M'13) received the M.S. degree in computer software and theory from East China University of Science and Technology, Shanghai, China, in 2008. He is currently working toward the Ph.D. degree with the Department of Electronic Engineering, Shanghai Jiao Tong University, Shanghai.

His research interests include digital image forensics and image processing.

Shilin Wang (M'12) received the B.Eng. degree in electrical and electronic engineering from Shanghai Jiao Tong University, Shanghai, China, in 2001 and the Ph.D. degree from the Department of Computer Engineering and Information Technology, City University of Hong Kong, Hong Kong, in 2004.

He has been with the School of Information Security Engineering, Shanghai Jiao Tong University, since 2004, where he is currently an Associate Professor. His biography is listed in Marquis *Who's Who in Science and Engineering*. His research interests include image processing and pattern recognition.

Shenghong Li (M'12) received the B.Eng. and M.S. degrees in electrical engineering from Jilin University of Technology, Changchun, China, in 1993 and 1996, respectively, and the Ph.D. degree in radio engineering from Beijing University of Posts and Telecommunications, Beijing, China, in 1999.

He has been with Shanghai Jiao Tong University, Shanghai, China, as a Research Fellow, an Associate Professor, and a Professor, since 1999. In 2010 he was a Visiting Scholar with Nanyang Technological University, Singapore. He has authored over 80 papers and co-authored four books. His research interests include information security, signal and information processing, artificial intelligence. He holds five granted patents.

Dr. Li was elected as a New Century Talent of the Chinese Education Ministry, Shanghai Dawn Scholar, and Marquis *Who's Who in the World*, in 2006, 2007, and 2009, respectively. He received the Prize of Shanghai Science and Technology Progress in China in 2003.

Jianhua Li received the Ph.D. degree in electronic engineering from Shanghai Jiao Tong University, Shanghai, China, in 1998.

He has been with the School of Information Security Engineering, Shanghai Jiao Tong University, since 2000, where he is currently a Professor. His research interests include information security and computer communication network.